A Respiratory Motion Prediction Based on Time-Variant Seasonal
Autoregressive Model for Real-Time Image-Guided Radiotherapy   77

78   Frontiers in Radiation Oncology

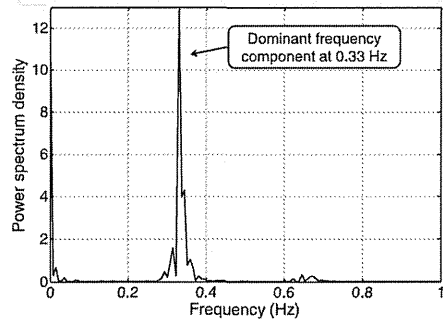**Figure 5.** An example of time series of lung tumor motion.

Figure 6. Power spectrum density of the respiratory induced tumor motion shown in Figure 5. The dominant frequency component is found at 0.33 Hz.

corresponding to the respiratory cycle can be found at 0.33 Hz approximately in this example. This means that the tumor motion has a periodical component induced by the 3 s respiratory cycle in average.

As is clear from the analysis, one of dominant components in respiratory motion is periodic variation due to repetition of inhalation and exhalation. However, the period of the motion is not constant, but a time varying function. Such quasi-periodical nature of the motion is simply found as fluctuation of peak-to-peak intervals. For example, time interval between a peak and next peak differs each other even if the amplitude variation is sufficiently small as shown in Figure 7. This suggests that the dominant frequency is time-varying.

Recalling that the breathing period is time-variant, short-time Fourier transform (STFT), instead of the normal long-time Fourier transform, was performed on the motion example. The time-variation of the frequency spectrum is shown in Figure 8. The dominant frequency at each time is depicted as black dashed line. The line clearly indicates that the respiratory cycle fluctuates with time. The range of the fluctuation was from 0.298 to 0.360 Hz in this example.
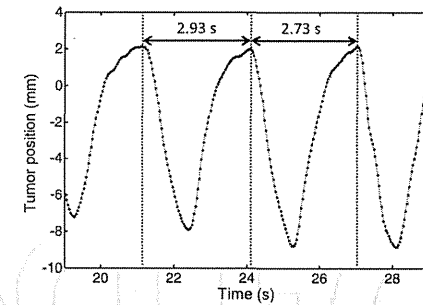

Figure 7. An example of fluctuated periodicity of respiratory motion. The peak to peak intervals indicated as double-headed arrows are not same to each other.
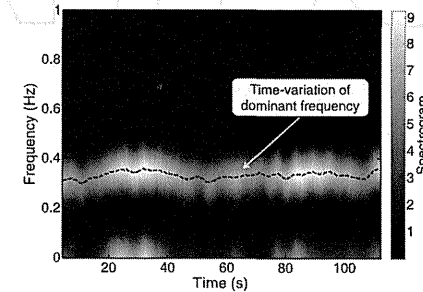

Figure 8. Time-variation of power spectrum density. The dominant frequency fluctuates with time. The range of fluctuation is from 0.298 to 0.360 Hz in this example.

3. Prediction methods

The periodicity found in the respiratory motion is a typical one of nonlinear and complex nature but also it can be useful to predict itself. That is, the past observed patterns in the motion will repeatedly arise at constant period. In this section, seasonal autoregressive (SAR) model is explained as a method with use of periodicity. Also, a limitation of general SAR model for lung tumor motion prediction is shown. Then, time-variant SAR model is introduced as a method designed for tumor motion prediction.

3.1. Seasonal autoregressive (SAR) model

Seasonal autoregressive integrated moving-average (SARIMA) model [22] is a general expression of the time series which changes periodically (i.e., a periodical function of time such that $x(t) \sim x(t - \rho \cdot s)$).

The SARIMA model of the time series $\{x(0), x(1), \ldots, x(T)\}$ with period s sample can be expressed as follows.

$$\phi(B)\Phi(B^s)(1 - B)^d(1 - B^s)^D x(t) = \theta(B)\Theta(B^s)\epsilon(t) \tag{1}$$

where d and D are respectively the order of local and seasonal integrated components, $\epsilon(t)$ is the Gaussian noise of which mean and variance are 0 and σ^2, respectively, and B is a delay operator defined by

$$B^k x(t) = x(t-k), \quad k = 1, 2, \ldots \quad (2)$$

Then, each components of the SARIMA model are given as follows.

$$\text{Autoregressive: } \phi(z) = 1 - \phi_1 z - \cdots - \phi_p z^p \quad (3)$$

$$\text{Moving-average: } \theta(z) = 1 + \theta_1 z + \cdots + \theta_q z^q \quad (4)$$

$$\text{Seasonal AR: } \Phi(z) = 1 - \Phi_1 z - \cdots - \Phi_P z^P \quad (5)$$

$$\text{Seasonal MA: } \Theta(z) = 1 - \Theta_1 z + \cdots + \Theta_Q z^Q \quad (6)$$

where p, q, P and Q are the orders of four components in (3)-(6) respectively.

The SARIMA model can express various periodical time series by designing the model parameters. In the followings, let us consider only the seasonal autoregressive (SAR) component to avoid the over fitting problem and to simplify the explanation of the prediction method. That is, let $p = q = Q = d = D = 0$ in (1), then for this special case, we can obtain SAR model for the time series $y(t)$ as follows.

$$y(t) = \epsilon(t) + \sum_{\rho=1}^{P} \Phi_\rho \cdot y(t - \rho \times s) \quad (7)$$

where P is the order of the SAR components, $\Phi_\rho, \rho = 1, 2, \ldots, P$ are the SAR coefficients, and s are the constant period of the target time series.

Then, to substitute $t + h$ for t, the prediction equation by using (7) can be given by

$$\hat{y}(t + h | t) = \sum_{\rho=1}^{P} \Phi_\rho \cdot y(t + h - \rho \times s) \quad (8)$$

where $\hat{y}(t + h | t)$ is the predicted value of future time $t + h$ samples with h samples ahead of current time t, and the term $-\rho \times s + h$ must be not longer than 0 for composing the prediction by using only past observations.

The equations (7) and (8) show that an essential core of the general SAR depends on an assumption that each values of the same phase correlate each other. These equations can provide a simple description with a single model for the periodical variation with period s. For example, if target time series are given by the following deterministic and fully periodical function:

$$x(t) = A_0 + \sum_{n=1}^{N} A_n \cdot \cos\left(2\pi \frac{n}{s} t - \varphi_n\right) \quad (9)$$

where $A_n, n = 0, 1, 2, \ldots$ and $\varphi_n, n = 1, 2, 3, \ldots$ are amplitudes and initial phases for each n-th harmonic component, respectively. Then, let $\Phi_\rho = 1/P$ in Eq. (8), the SAR model can well
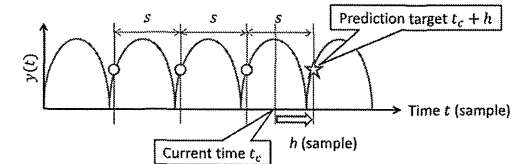
Figure 9. Schematic diagram of SAR model-based prediction for time series with constant period.
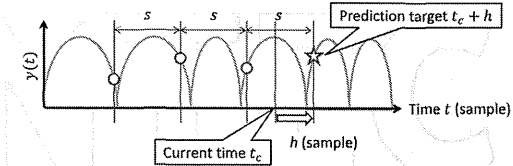

Figure 10. Schematic diagram of SAR model-based prediction for time series with fluctuated period.

predict the future value of the periodical function $x(t + h)$ at h-sample ahead future as follows.

$$
\begin{aligned}
\hat{x}(t + h | t) &= \frac{1}{P} \sum_{\rho=1}^{P} \left(A_0 + \sum_{n=1}^{N} A_n \cdot \cos\left(2\pi \frac{n}{s}(t + h - \rho \cdot s) - \varphi_n\right) \right) \\
&= \frac{1}{P} \sum_{\rho=1}^{P} \left(A_0 + \sum_{n=1}^{N} A_n \cdot \cos\left(2\pi \frac{n}{s}(t + h) - 2\pi\rho - \varphi_n\right) \right) \\
&= \frac{1}{P} \sum_{\rho=1}^{P} \left(A_0 + \sum_{n=1}^{N} A_n \cdot \cos\left(2\pi \frac{n}{s}(t + h) - \varphi_n\right) \right). \quad (10)
\end{aligned}
$$

Figure 9 shows a schematic diagram of SAR model-based prediction for simple periodic time series with period s. In this example, SAR model can predict the target value (drawn as star) by referring the past observed values (drawn as circles) which are similar to the target value by using constant period s.

As shown by the prediction example, the SAR model-based equation (8) is useful and powerful to predict unknown future value of periodic time series. Then, remember that the dominant component in respiratory tumor motion is periodical component. These facts suggest that the SAR model is suitable to predict the tumor motion. However, remember that the periodicity in our target time series, lung tumor motion, fluctuates. The use of constant period s in equation (8) may be improper for the tumor motion. That is, if the periodical nature in the target time series changes with time, the constant period will provide a large prediction error.

A simple solution for adapting the SAR model to the fluctuated periodicity is to substitute a time-variant period $s(t)$ for the constant period s given by

$$\hat{y}(t) = \epsilon(t) + \sum_{\rho=1}^{P} \Phi_\rho \cdot y(t - \rho \cdot s(t)). \quad (11)$$

Then the new prediction equation is written as

$$\hat{y}(t + h|t) = \sum_{p=1}^{P} \Phi_p \cdot y(t + h - \rho \cdot s(t + h)). \tag{12}$$

The equation above is about the same to the SAR model-based method [19] and it seems that it can adapt to the fluctuated periodicity, but this simple extension of SAR model has a limitation.

For explanation of the limitation, let us consider time series with a time-varying period as a function of time t. For this situation, the instantaneous phase $\vartheta(t)$ of the time series is given as a time-integration of the angular velocity $\omega(t)$, such as $\vartheta(t) = \int_0^t \omega(t) dt$. If the angular velocity is given as a linear function of time t,

$$\omega(t) = \omega_a t + \omega_0, \tag{13}$$

where ω_a and ω_0 are constants. And the instantaneous phase is given a nonlinear (the second-order in this case) function as

$$\vartheta(t) = \frac{1}{2}\omega_a t^2 + \omega_0 t. \tag{14}$$

Then let us assume that $s(t)$ is known or estimated correctly. That is, the term $s(t)$ can refer the instantaneous phase same to the target time t, i.e., $\vartheta(t) = \vartheta(t - s(t))$ However, the terms $\rho \cdot s(t), \rho = 2, 3, \ldots, P$ in (11) cannot refer the same instantaneous phase, i.e., $\vartheta(t) \neq \vartheta(t - \rho \cdot s(t)) + 2\pi\rho$, even if the $s(t)$ is given as a true value.

Thus, the simple SAR model-based solution by using the time-varying period $s(t)$ cannot express the fluctuated periodic nature suitably, even if the change of the periodicity is sufficiently simple such as a linear function of time. This is one of the limitations of SAR model in the prediction of fluctuated periodical time series such as respiratory tumor motion.

3.2. Time-variant SAR (TVSAR) model

To overcome the limitation of the general SAR model, a time-variant SAR (TVSAR) model for prediction of the lung tumor motion has been proposed [21]. The TVSAR equation corresponding to (7) can be expressed as

$$y(t) = \epsilon(t) + \sum_{p=1}^{P} \Phi_p \cdot y(t - r_p(t)). \tag{15}$$

where $r_p(t)$ are reference intervals of the pth order at time t.

The reference intervals $r_p(t)$ can be defined as a time interval between the current time and the corresponding past time which has the same phase to the current one. In other words, if an instantaneous phase $\vartheta(t)$ of the time series is given, the reference intervals can be defined as follows.

$$r_p(t) = \arg\min_{k>0} |\vartheta(t) - 2p\pi - \vartheta(t - k)| \tag{16}$$
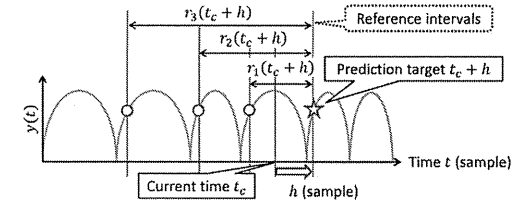

Figure 11. Schematic diagram of time-variant SAR (TVSASR) model-based prediction for time series with fluctuated period.
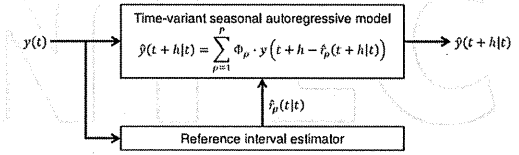

Figure 12. Schematic diagram of TVSAR model-based prediction system.

Also, if the period is a constant, the reference interval can be expressed by

$$r_p(t) = \rho \times s, \text{ if } \frac{d\vartheta(t)}{dt} = \frac{2\pi}{s}. \tag{17}$$

Note that, the constant reference interval shown by (17) corresponds to that used in the general SARIMA equations of (7) and (8).

Then, an ideal prediction equation of the time-variant SAR is expressed by substituting $t + h$ for t as follows.

$$\hat{y}(t + h|t) = \sum_{p=1}^{P} \Phi_p \cdot y(t + h - r_p(t + h)) \tag{18}$$

where the term $h - r_p(t + h) \leq 0$.

Figure 11 shows a schematic diagram of TVSAR model-based prediction. The reference intervals can refer the past values observed which are corresponding to the target value, on the time series with fluctuated period. Also, Figure 12 shows TVSAR model-based prediction system.

Note that, in (18), we have to know the reference interval at h sample ahead future, but it is unknown in practice. In this case, we need to estimate it. The estimation method will be explained in the next section.

3.2.1. Online estimation of reference intervals: Short-time correlation analysis

In TVSAR model, the reference interval $r_p(t)$ is an important factor to predict the lung tumor motion accurately, and must be estimated on-line. In this study, a correlation analysis is adopted to estimate the reference interval.

The correlation analysis based estimation procedure of the reference interval is as follows.

A Respiratory Motion Prediction Based on Time-Variant Seasonal
Autoregressive Model for Real-Time Image-Guided Radiotherapy 83

84 Frontiers in Radiation Oncology

1. Calculate a correlation function between the latest subset

$$\{y(t-w), y(t-w+1), \ldots, y(t-1), y(t)\} \tag{19}$$

and k-sample lagged subset

$$\{y(t-k-w), y(t-k-w+1), \ldots, y(t-k-1), y(t-k)\} \tag{20}$$

where w is a window length for subset time series. The correlation function is given by

$$\gamma(t,k) = \frac{1}{w} \sum_{j=0}^{w-1} \frac{y(t-j) - \mu_t}{\sigma_t} \frac{y(t-k-j) - \mu_{t-k}}{\sigma_{t-k}} \tag{21}$$

Here μ_t and σ_t are the sample mean and standard deviation of the subset time series.

2. The estimated reference intervals $\hat{r}_\rho(t|t)$ can be obtained by the intervals between $k = 0$ and the peak points of the correlation function $\gamma(t,k)$ corresponded to each seasonal order ρ:

$$\hat{r}_\rho(t) = \arg \max_{r_\rho(t-1)-l \leq k \leq r_\rho(t-1)+l} \gamma(t,k) \tag{22}$$

where l defines the search area for the peak of $\gamma(t,k)$.

3. The window length is updated at each time by using the latest estimation of the first order reference interval as

$$w = \text{round}(0.5\hat{r}_1(t|t)). \tag{23}$$

Note that the windows length can affect the accuracy and response time to estimate the fluctuated periodicity. In this study, the window length was empirically set as almost half of single wave.

The initial condition is defined as follows.

$$\hat{r}_\rho(1|1) = \rho \times \bar{s}, \tag{24}$$

$$w = \text{round}(0.5\hat{r}_1(1|1)) \tag{25}$$

where $\bar{s}$ is the average of pre-observed time variant periods of the time series. $\bar{s} = 90$ sample was used for this study.

An example of the correlation function and estimated reference intervals are shown in Figure 13. The reference intervals are thus estimated as intervals from lag 0 to ρ-th local maximum points of the correlation function.

Time-variation of the correlation function and estimated reference intervals are shown in Figure 14. As is clear from this figure, reference intervals of lung tumor motion intricately change with time evolution.

We can now estimate the reference intervals, but we need future value of them for (18). According to the figure 14, these reference intervals also fluctuate intricately and those prediction is difficult. So $r_\rho(t+h)$ cannot be directly used for the prediction in (18). As a realistic way, we simply extrapolated $r_\rho(t+h)$ from the current estimation $\hat{r}_\rho(t|t)$ with zero-order hold: $\hat{r}_\rho(t+h|t) = \hat{r}_\rho(t|t)$. Then, (18) can be rewritten as

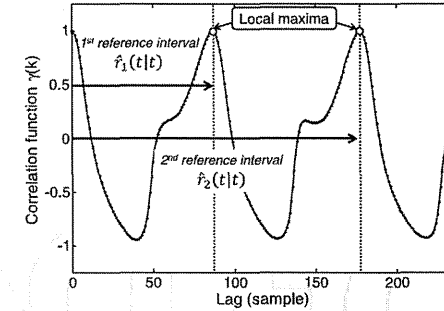$$\hat{y}(t+h|t) = \sum_{\rho=1}^{P} \Phi_\rho \cdot y(t+h-\hat{r}_\rho(t|t)). \tag{26}$$

Figure 13. An example of the correlation function $\gamma(t,k)$ and estimeted reference intervals $r_\rho(t), \rho = 1$ and 2 for the tumor motion shown in Figure 5.
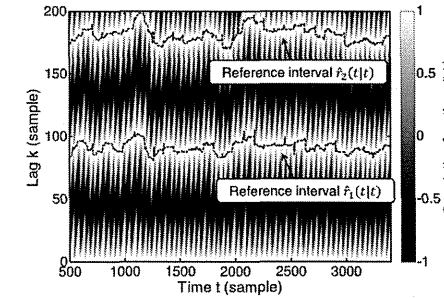

Figure 14. Time-variation of the correlation function $\gamma(t,k)$ and estimated reference intervals $r_\rho(t), \rho = 1$ and 2 for the tumor motion shown in Figure 5.

4. Experimental results

To evaluate the prediction performance of the methods described in Section 3, a prediction experiment by using clinical data sets was performed.

4.1. Experimental setup

4.1.1. Clinical data sets of lung tumor motion

Three data sets of respiratory tumor motion time series were used for the experiment. All the data sets were observed with sampling frequency $F_s = 30$ Hz and provided by Hokkaido University Hospital. Note that, a part of the data sets and measuring condition have been already shown in Section 2. Each data sets include three time series that correspond to spatial axes; left-right (LR), superior-inferior (SI), and anterior-posterior (AP) axes, respectively. The observational noises included in original data sets were preliminarily eliminated by using the statistical and low-pass filters. Figure 15 shows the three data sets and Table 1 summarizes data sets characteristics.
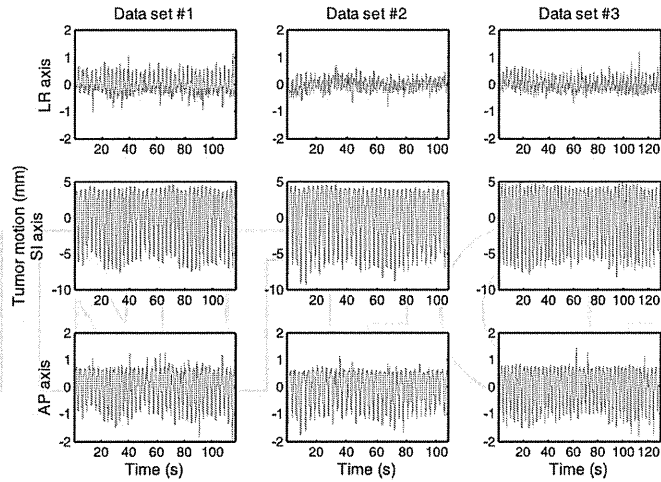
Figure 15. Three data sets of lung tumor motion. Each rows correspond to LR: left-right, SI:
superior-inferior, and AP: antero-posterior axes.

4.1.2. Tested methods

For comparison of the prediction performance, the following four methods were tested.

1. Zero-order hold (ZOH) method assumes that the latest position of tumor will not change
   in future. The prediction equation is given by

$$\hat{y}(t + h|t) = y(t). \tag{27}$$

Note that the use of ZOH corresponds to the case that the system latency in radiotherapy
machine is not compensated.

2. First-order hold (FOH) method assumes that the latest position and velocity will not
   change in future. The prediction equation is given by

$$\hat{y}(t + h|t) = y(t) + (y(t) - y(t - 1)) h. \tag{28}$$

3. Seasonal autoregressive (SAR) model-based prediction given in (12). Note that the
   time-variant period is given as $s(t + h) = \hat{r}_1(t|t)$.

Case #	Range of motion (mm)			Length	Evaluation coverage		Average period
	LR	SI	AP	T samples	t_s	t_e	$\bar{s}$
#1	0.7	10.2	1.5	3500 (116.7 s)	500 (16.7 s)	3500 (116.7 s)	91 (3.034 s)
#2	0.4	11.0	1.6	3228 (107.6 s)	501 (16.7 s)	3228 (107.6 s)	89 (2.968 s)
#3	0.5	10.9	1.6	3900 (130.0 s)	502 (16.7 s)	3900 (130.0 s)	91 (3.034 s)

Table 1. Brief summary of tested data sets. Range of motion is average distance from exhalation to
inspiration.

4. Time-variant SAR (TVSAR) model-based prediction given in (26).

Parameters for SAR and TVSAR models are summarized in Table 2.

4.1.3. Performance indexes

To evaluate the prediction performance, mean absolute error (MAE) was calculated. MAE is
given as a function of prediction horizon h as follows.

$$\text{MAE}(h) = \frac{1}{t_e - t_s} \sum_{t=t_s}^{t_e} |e(t + h|t)| \tag{29}$$

Here t_s and t_e are lower and upper bounds for the evaluation shown in Table 1, and $e(t + h|t)$
is a prediction error defined by the Euclidean distance between the actual position and the
predicted position.

The prediction error is calculated as follows.

$$e(t + h|t) = \sqrt{\sum_{i=1}^{3} (\hat{y}_i(t + h|t) - y_i(t + h))^2} \tag{30}$$

where $i = 1, 2$ and 3 denote LR, SI, and AP directions, respectively.

In addition to MAE, prediction success rate was adopted to evaluate the prediction efficiency
for short treatment time. While treatment, the irradiation must be interrupted when
unacceptable distance between the irradiated field and the target volume is detected for
patient safety. Then, frequent prediction failure may prolong the treatment fraction. Thus,
the rate of prediction success can discover better method. The prediction success rate (PSR) is
defined as follows.

$$\text{PSR}(h) = \frac{\text{Number of successfully predicted samples}}{\text{Number of all evaluated samples}} \tag{31}$$

where the numerator is calculated as the number of the prediction errors within a threshold
for tolerant accuracy. In this study, the threshold was set as 1 mm.

4.2. Results

Figure 16 shows 15 samples (0.5 s) forward prediction examples of tested methods. This
examples were performed on SI direction of the data set #1. According to the prediction
examples, SAR and TVSAR predictions seems smooth and similar to the actual position. Their
errors are around zero, but sometimes the errors become larger than 2 mm. Also, there is a

Parameters	
Order P	2
Coefficients $\Phi_\rho, \rho = 1, 2, \dots, P$	$1/P$
Maximum lag for correlation function	400

Table 2. Parameters for SAR and TVSAR models

A Respiratory Motion Prediction Based on Time-Variant Seasonal
Autoregressive Model for Real-Time Image-Guided Radiotherapy 87
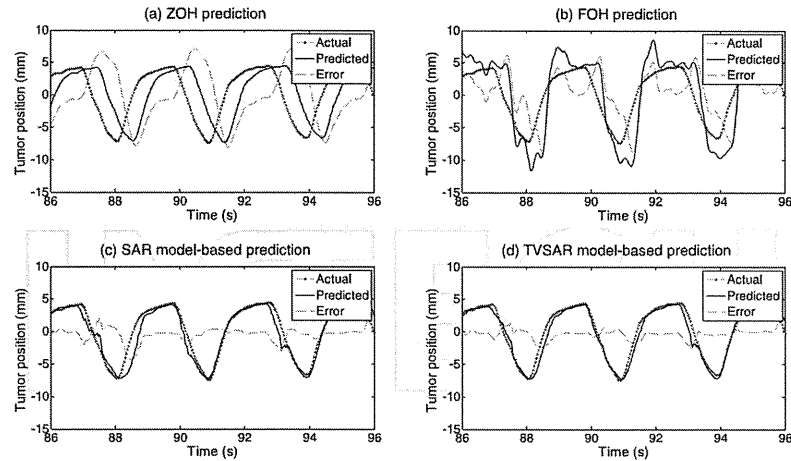
88 Frontiers in Radiation Oncology

Figure 16. Examples of 0.5 s forward future prediction. (a) Zero-order hold, (b) First-order hold, (c) Seasonal autoregressive model, and (d) Time-variant seasonal autoregressive model. Gray dots, black lines, dashed lines denote actual position, predicted position, and distance between the actual and predicted positions.

Figure 17. Mean absolute error as a function of prediction horizon h/F_s (s).

Figure 18. Prediction success rate as a function of prediction horizon h/F_s (s).

difference between SAR and TVSAR predictions at 87 to 89 s. Thus, TVSAR has provided better prediction. On the other hand, ZOH and FOH predictions are noisy and not fitted into the actual position. Their errors are frequently larger than 5 mm.

Figures 17 and 18 show MAE and PSR as a function of prediction horizon h/F_s (s). Each curves of prediction performances drawn in the figures are averaged over the data sets. Also, error bars indicates standard deviation of each performances for data sets variation.

As is clear from the figures, TVSAR is superior to SAR constantly. This suggests that the basic concept of the TVSAR is more proper than SAR for the lung tumor motion prediction, i.e., reference intervals can work to improve the prediction accuracy for quasi-periodical nature. Then, MAE and PSR curves of TVSAR are the least and the highest for prediction horizon $h/F_s > 0.2$ s, respectively. It means that TVSAR is the first best method in the tested methods for the radiotherapy machine with system latency of 0.2 s or longer. The average accuracy and 70 % of the predicted samples respectively are sub-millimeter. This may suggest that the TVSAR can perform tumor following irradiation during over 70 % of a single treatment fraction.

SAR is the second-best, but the average error for prediction horizon longer than 0.5 s is over 1 mm. Note that the difference from TVSAR depends on the use of the second reference interval in this experiment. Thus, unsuitable referring the past values by using the latest period, $\rho \cdot s(t)$, increases the considerable prediction error.

ZOH and FOH are superior to SAR and TVSAR predictions for shorter prediction horizons < 0.2 s. It is not remarkable because the position and velocity don't change drastically in short term in general. The periodicity in the respirato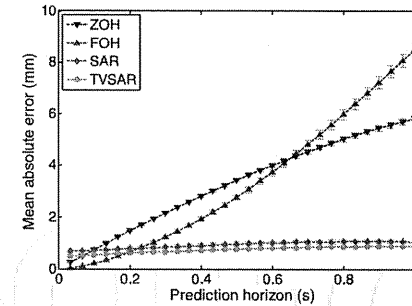ry motion quickly changes the position and velocity at each peaks. Then ZOH and FOH cannot take into account the changes arisen. Therefore, their prediction errors drastically increase to unacceptable level with increase in prediction horizon. Those frequent and large prediction errors cause prolong the treatment fraction.
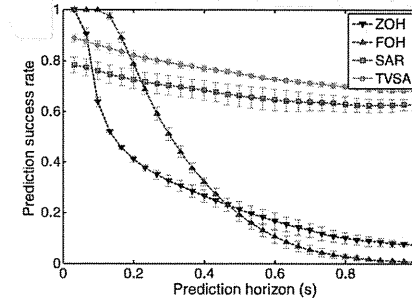
5. Conclusion

In this chapter, a prediction method of respiratory induced tumor motion for tumor following radiotherapy were introduced. The respiratory motion involves quasi-periodic nature as a dominant component and the motion causes unacceptable error of irradiation due to the system latency between tumor localization and beam-repositioning. To compensate the latency, prediction method of respiratory motion is very important and its prediction accuracy directly affects irradiation accuracy. Then, as a potent prediction method, time-variant seasonal autoregressive (TVSAR) model was introduced. TVSAR is an extended model of seasonal autoregressive model to be adaptable to the quasi-periodical nature. An experimental result by using clinical data sets of lung tumor motion showed the average accuracy of TVSAR is less than 1 mm for up to 1 s forward prediction and TVSAR is superior to other methods tested for <0.2 s ahead future prediction. Thus, TVSAR model-based prediction

method achieved accurate prediction of the respiratory tumor motion and can help the tumor
following irradiation.

Acknowledgements

Author details

Kei Ichiji
*Department of Electrical and Communication Engineering, Graduate School of Engineering, Tohoku
University, Sendai, Japan.*
Research fellow of Japan Society for the Promotion of Science (JSPS).

Noriyasu Homma and Makoto Yoshizawa
*Research division of Advanced Information Technology, Cyberscience center, Tohoku University,
Sendai, Japan.*

Masao Sakai
Center for Information Technology in Education, Tohoku University, Sendai, Japan.

Makoto Abe
*Department of Electrical and Communication Engineering, Graduate School of Engineering, Tohoku
University, Sendai, Japan.*

Norihiro Sugita
*Department of Management Science and Technology, Graduate School of Engineering, Tohoku
University, Sendai, Japan.*

6. References

[1] Onishi H, Araki T, Shirato H, Nagata Y, Hiraoka M, Gomi K, et al. Stereotactic
hypofractionated high-dose irradiation for stage I nonsmall cell lung carcinoma:
clinical outcomes in 245 subjects in a Japanese multiinstitutional study. Cancer.
2004;101(7):1623–1631.

[2] Shirato H, Suzuki K, Sharp G, Fujita K, Onimaru R, Fujino M, et al. Speed and
amplitude of lung tumor motion precisely detected in four-dimensional setup and
in real-time tumor-tracking radiotherapy. International journal of radiation oncology,
biology, physics. 2006;64(4):1229–1236.

[3] Suh Y, Dieterich S, Cho B, Keall P. An analysis of thoracic and abdominal tumour
motion for stereotactic body radiotherapy patients. Physics in medicine and biology.
2008;53(13):3623–3640.

[4] Keall P, Mageras G, Balter J, Emery R, Forster K, Jiang S, et al. The management of
respiratory motion in radiation oncology report of AAPM Task Group 76. Medical
physics. 2006;33(10):3874–3900.

[5] Purdy J. Current ICRU definitions of volumes: limitations and future directions.
Seminars in radiation oncology. 2004;14(1):27–40.

[6] Kubo H, Hill B. Respiration gated radiotherapy treatment: a technical study. Physics in
medicine and biology. 1996;41(1):83–91.

[7] Shirato H, Shimizu S, Kitamura K, Nishioka T, Kagei K, Hashimoto S, et al.
Four-dimensional treatment planning and fluoroscopic real-time tumor tracking
radiotherapy for moving tumor. International journal of radiation oncology, biology,
physics. 2000;48(2):435–442.

[8] Keall P, Kini V, Vedam S, Mohan R. Motion adaptive x-ray therapy: a feasibility study.
Physics in medicine and biology. 2001;46(1):1–10.

[9] Poulsen P, Cho B, Sawant A, Ruan D, Keall P. Detailed analysis of latencies in
image-based dynamic MLC tracking. Medical physics. 2010;37(9):4998–5005.

[10] Poulsen P, Cho B, Ruan D, Sawant A, Keall P. Dynamic multileaf collimator tracking of
respiratory target motion based on a single kilovoltage imager during arc radiotherapy.
International journal of radiation oncology, biology, physics. 2010;77(2):600–607.

[11] Sharp G, Jiang S, Shimizu S, Shirato H. Prediction of respiratory tumour
motion for real-time image-guided radiotherapy. Physics in medicine and biology.
2004;49(3):425–440.

[12] Ma L, Herrmann C, Schilling K. Modeling and prediction of lung tumor motion for
robotic assisted radiotherapy. Intelligent Robots and Systems, 2007 IROS 2007 IEEE/RSJ
International Conference on. 2007;p. 189–194.

[13] Bukovsky I, Ichiji K, Homma N, Yoshizawa M, Rodriguez R. Testing potentials of
dynamic quadratic neural unit for prediction of lung motion during respiration for
tracking radiation therapy. Neural Networks (IJCNN), The 2010 International Joint
Conference on. 2010;p. 1–6.

[14] Mizuguchi A, Demachi K, Uesaka M. Establish of the prediction system of chest
skin motion with SSA method. International Journal of Applied Electromagnetics and
Mechanics. 2010;33(3):1529–1533.

[15] Ruan D. Kernel density estimation-based real-time prediction for respiratory motion.
Physics in medicine and biology. 2010;55(5):1311–1326.

[16] Kalet A, Sandison G, Wu H, Schmitz R. A state-based probabilistic model for tumor
respiratory motion prediction. Physics in medicine and biology. 2010;55(24):7615–7631.

[17] Verma PS, Wu H, Langer MP, Das IJ, Sandison G. Survey: Real-Time Tumor
Motion Prediction for Image-Guided Radiation Treatment. Computing in Science &
Engineering. 2011;13(5):24–35.

[18] Box G, Jenkins G, Reinsel G. Time series analysis. Holden-day San Francisco; 1976.

[19] Homma N, Sakai M, Endo H, Mitsuya M, Takai Y, Yoshizawa M. A new
motion management method for lung tumor tracking radiation therapy. WSEAS
TRANSACTIONS on SYSTEMS. 2009;8(4):471–480.

[20] McCall K, Jeraj R. Dual-component model of respiratory motion based on the periodic
autoregressive moving average (periodic ARMA) method. Physics in medicine and
biology. 2007;52(12):3455–3466.

[21] Ichiji K, Sakai M, Homma N, Takai Y, Yoshizawa M. SU HH BRB 10: Adaptive
Seasonal Autoregressive Model Based Intrafractional Lung Tumor Motion Prediction
for Continuously Irradiation. Medical Physics. 2010;37.

[22] Brockwell P, Davis R. Introduction to time series and forecasting. Springer Verlag; 2002.

Chapter 3
Touch Feelings and Sensor for Measuring the Touch Feeling

Mami Tanaka

Abstract Touch feelings and tactile sense play very important role in our daily life. However, the mechanism has not clarified yet. In this chapter, the receptor in human skin and haptics that is motion of hand/finger will be introduced. And the sensory experiments and measurement were carried out in order to clarify the mechanism of rough and soft feelings which are fundamental touch feelings and the developed sensor for measuring tactile sensation for fabrics and the palpation sensor for measuring prostatic glands will be introduced.

3.1 Introduction

Touch is one of five senses, and it can feel mechanical stimuli (pressure, vibration, heat, cold, pain, etc.) through the skin. Skin is the largest sense organ in the human body and the area is about 1.8 m^2 in the average adult [1]. Unborn babies have the skin function from the 9th week after conception and babies use their hands and mouth in order to obtain the many information of outside world.

Touch is active and passive and it is ruled under the law of action and reaction of skin and objects, which is called "third law of motion". This point is very unique and tactile sense is unlike other senses for this point. Therefore, it is difficult to clarify the mechanisms of tactile sense and the feeling of touch. The mechanisms of vision and hearing have been already clarified and the principals contribute the development of the glasses and hearing aid in order to assist the vision and hearing sense, respectively. It is very important to clarify the mechanism of the touch sense, like these.

M. Tanaka (✉)
Department of Biomedical Engineering, Tohoku University, Sendai 980–8579, Japan
e-mail: mami@rose.mech.tohoku.ac.jp

Table 3.1 Sensory receptor and modality and categorization in human skin [1]

Receptor	Modality	Category
Meissner's corpuscle	Touch flutter	FAI
Pacinian corpuscle	Touch vibration	FAII
Merkel's discs	Touch pressure	SAI
Ruffini endings	Touch pressure	SAII
Free nerve endings	Temperature and pain	

3.2 Sensory Receptor in Human Skin

Table 3.1 shows the sensory receptors and modality in human skin [1]. Free nerve endings react for temperature and pain and they are different from the others. The other receptors react to mechanical stimuli and are classified depending on the reaction speed, fast adaptive (FA) and slow adaptive (SA). In addition the receptors are classified depending on the size of area, the area of II means larger than that of I.

As the FA sensory receptors, there are two kinds, Pacinian corpuscle and meissner's corpuscle. Concerning with these FA sensory receptors, they have higher sensitivity frequency ranges. When the receptors receive the sinusoidal wave stimulus, Pacinian corpuscle can react under 1 μm threshold at 250–300 Hz, and Meissner's can react under 10 μm at 30–40 Hz. It is interesting the receptors have different higher frequency ranges.

3.3 Search for the Mechanism About Roughness and Softness

There are various fields to use touch feelings and sensation, for example, to make something in industry, palpation in medical and welfare fields.

In industry, the sensory tests usually are done to evaluate the many things, but a huge number of subjects are needed to obtain the accurate touch sensation. Therefore, the training of the expert for measuring touch feelings is important. Palpation has important role for a clinician/doctor in diagnoses. They assess smoothness, roughness, and softness of an area of patient and/or find the abnormal point such as hard spot by palpation. However, palpation using human's fingers is said to be ambiguous, subjective and much affected by their experience. From these points, it is not easy to share the information of a same diagnosis.

Various kinds of information are obtained as the touch feeling and the roughness and softness are fundamental touch feelings. The physical value of the roughness can be measured by surface roughness measuring instrument as the amplitude of the surface asperity, but the measurement object is limited such as metallic materials and the relationship between the obtained physical value and the touch feeling has not been clarified. In addition, there is not only the hard one like the

metal but also various one in the world where we live. These make more difficult the clarification of the mechanism that human feel rough.

The softness of the object is also measured as the stiffness and Young's modulus by hardness tester, but the relation between the values and touch feeling has not been clarified. Therefore, the clarification of the mechanism becomes more difficult.

In order to search the trigger of the mechanism, we investigated the relations between amplitude and frequency information, and smoothness and roughness.

3.4 Tactile Display for the Roughness Tests

A simple tactile display that subjects can touch and feel various degree of smoothness is developed. Bimorph cell is used as an actuator to generate vibratory stimulus. And the display can adjust the frequency of vibratory stimulus. Through two experiments, the relationships between the frequency distribution of vibratory stimulus and smoothness feelings are investigated.

After this, "roughness" and "smoothness" do not mean physical roughness and smoothness of an object, but mean sensuous roughness and smoothness which human feels using their tactile sense.

A simple tactile display using bimorph cells is fabricated. The tactile display is shown in Fig. 3.1. The display consists of an actuator on the display and it is vibrated using bimorph cells with steady frequency and amplitude. Three input waves of the bimorph cells are generated using GNU Octave which is numerical computation software. The generated waves are transmitted to the amplifier and the amplified outputs were applied to the actuators. In experiments, subjects put their forefingers of dominant hand on the actuators and evaluate what they feel. Figures 3.2 and 3.3 show the size of the display and experimental scene, respectively.

3.5 Sensory Tests for Roughness

Two sensory tests about roughness/smoothness are conducted using the tactile display. In the first experiment, the relations between the vibration frequency and "Kansei" keywords of roughness feeling were investigated and in the second

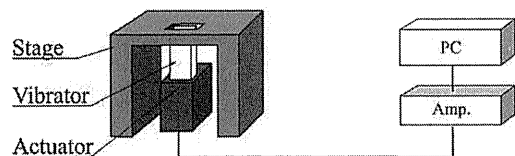Fig. 3.1 System of tactile display

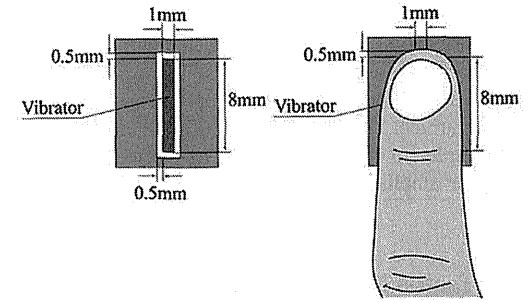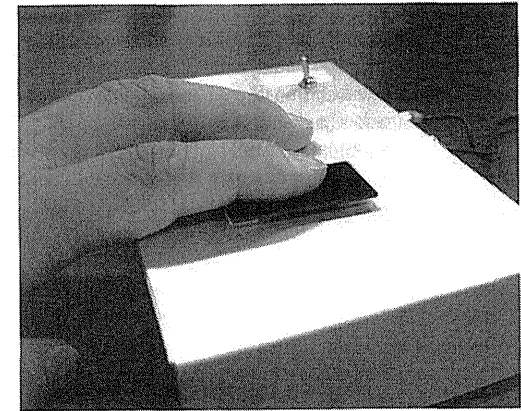Fig. 3.2 Size of the display


Fig. 3.3 Scene of the tests

experiment the relations between vibration frequency and degrees of roughness feeling were investigated.

In order to find the relations between the vibration frequency and "Kansei" words of roughness feeling, the various vibration stimuli are displayed to the subjects. In the experiment, the subjects touched the tactile display and selected one keyword from six Kansei keywords to answer how they felt it.

Six keywords are as follows. "A: not felt", "B: snaky", "C: uneven", "D: rough", "E: fine" and "F: vibration". The keywords were selected through the preliminary experiment. The subjects are six men and they are 21–32 years old. The tactile display was presented sinusoidal wave vibration stimulus of the amplitude 30 μm and the frequencies of the stimulus were changed from 1 to 250 Hz.

Figure 3.4 shows the ratio of number of subjects that use each keyword to express each stimulus. From this result, it is seen that each Kansei keyword has the corresponding frequency distribution. At the lowest frequency range, most of the subjects selected "not felt", and at the highest frequency range many subjects answered "vibration". At low frequency range, the subjects answered "snaky" and

Fig. 3.4 Ratio of number of subjects that use each keywords to express each stimuli. A: "not felt", B: "snaky", C: "uneven", D "rough", E "fine" and F "vibration"
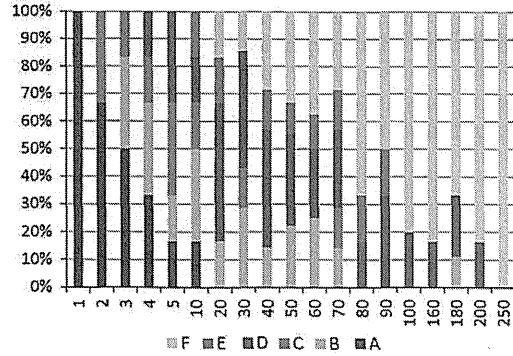
"uneven". Kansei keyword "roughness" can be felt at broad area from 4 to 200 Hz and "fine" can be felt under 100 Hz.

For the next experiment, the relationships between the frequency distribution of vibratory stimulus and smoothness/roughness are investigated. In the experiments, the input waves are used as the combination patterns (named p1 and p2) and one wave is displayed to the subject for 3 s, and after 0.2 s the other wave is displayed to the subject for 3 s, sequentially. After that, the subject evaluate smoothness/ roughness of p2 compared with p1 using the evaluation form with five grades as shown in Fig. 3.5.

In the experiments, the experiment orders are random and the displayed order of p1 and p2 are also. At the experimental time, the subjects don't know what the displayed stimuli are. The amplitude of the displayed stimuli is settled at 30 μm and the frequencies of the stimulus were changed from 1 to 250 Hz. The subjects are seven male and they are 21–32 years old.

By the Scheffe's pair comparison method [2], one of semantic differential methods, the scores of each wave pattern are obtained. Analysis results of pair comparison are shown in Fig. 3.6. Figure 3.6 shows score versus stimulus frequency, and the results are separated roughly into three groups. In the figures, the higher score means that human evaluate the displayed stimulus is rougher and the lower score means that human evaluate the displayed stimulus is smoother.

The subjects of the first group feel the roughest from 50 to 100 Hz, and those of the second group feel the roughest at about 200 Hz, and that of the last group feel the roughest twice at 50 and 200 Hz. These results are caused that Meissner's
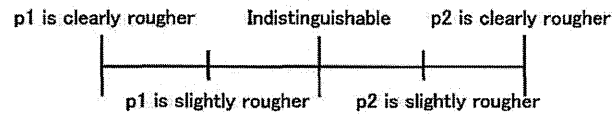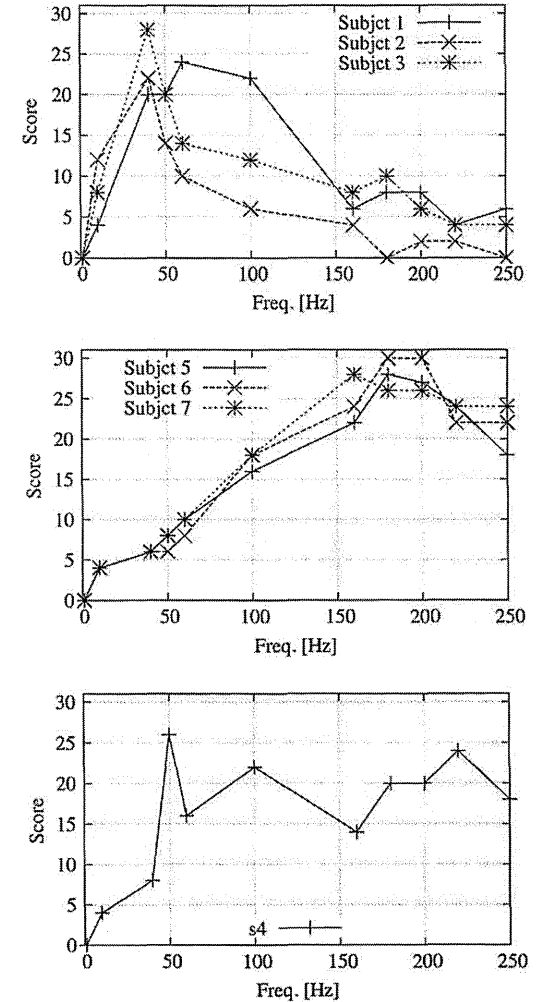

Fig. 3.5 Evaluation form of sensory test of the roughness

Fig. 3.6 Roughness score versus frequency

corpuscle and Pacinian corpuscle have the highest sensitivity frequency area around 50 and 200 Hz to the threshold for vibratory stimulus, respectively mentioned above [1]. And these results show that there are personal differences for the roughness feeling and the differences are considered to depend on whether Meissner's corpuscle or Pacinian corpuscle reacts.

In this experiment, the amplitude of the stimuli was settled constant. When the frequencies were settled constant and the amplitude of the stimulus were changed,

human touch feelings about roughness are investigated. It was confirmed that the roughness feelings increase with the increase of the amplitude of the stimuli. Moreover, we must consider the combination of amplitude and frequency, it is necessary to investigate the relations about amplitudes and frequencies in detail and to increase the number of subjects for the investigation of the influence of the individual variation.

3.6 Sensory Tests for Hardness

Next, the target is softness that is also one of fundamental touch feelings. The relationships between physical properties of soft objects and the tactile softness are investigated. After this, the tactile softness means touch feeling of softness when human touches an object. First, the relationship between the stiffness of measured objects and the tactile softness is investigated using silicone blocks with different Young's modulus.

To investigate the mechanism of evaluating tactile softness of human, the relationship between the stiffness of evaluated objects and tactile softness when human touch to the object and feel is investigated. In experiments, six kinds of silicone block objects with different Young's modulus are prepared. The dimensions of these objects are 30 mm width, 30 mm length, and 20 mm thickness. Young's modulus of them are 0.37, 0.82, 0.94, 1.01, 1.47, and 2.86×10^{-1} MPa. Young's modulus of the objects are determined by reference to Young's modulus of epidermis, dermis and hypodermis of skin [3–6].

Using these silicone objects, a sensory test of tactile softness is conducted. In an experiment, two objects are picked out of the six objects, and those are placed on the force sensor. Six subjects touch the objects using their forefinger alternately, and compared tactile softness of two objects. The subjects are 20–32 years old men. The force sensor can measure the contact force applied on the objects vertically when a subject touches the object. The sensory tests are conducted in total 15 combinations of the six objects. The results of sensory test were evaluated using Scheffse' paired comparison method [2].

The subjects answered which object is higher young's modulus, and the correct answer rate was almost 100 % in all trial, and it found that the tactile softness of the objects decrease with increase of Young's modulus of the objects. Young's modulus and stiffness of the objects mean the same tendency, because thickness of all objects are the same. It can be said that tactile softness of the objects decreases with increase of stiffness of the objects.

The contact force was applied to the objects by the subjects with their forefinger in the sensory test and it was recorded by the force sensor as shown Fig. 3.7. Figure 3.8 shows the scene of the sensory test, and one example of the force sensor output. The peak of the force is defined as the value of the contact force. The contact force is almost 5–15 N. In order to investigate the relation of hardness and contact force in detail, the difference and ratio are investigated.
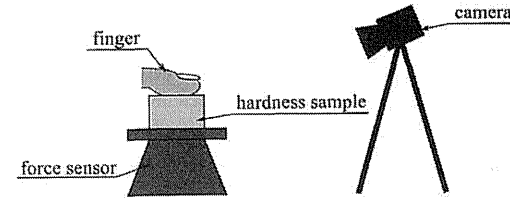
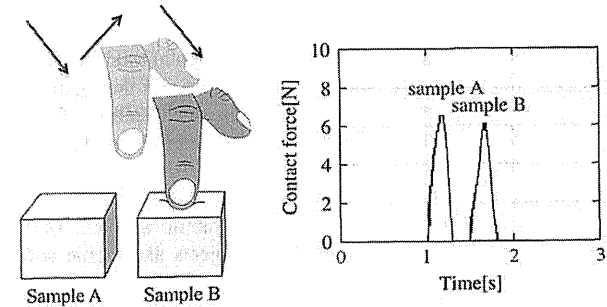Fig. 3.7 System setup for sensory test measuring hardness

Fig. 3.8 Scene of the sensory test for hardness and one example of the contact force sensor output

Figures 3.9 and 3.10 show the differences and ratio of the contact force between the compared two objects, respectively. Sample A is harder than sample B and the young's modulus is called Ea and Eb (Ea > Eb), and Fa and Fb are the peak force of samples A and B. The horizontal axis values are difference (Ea−Eb) and ratio (Ea/Eb) of Young's modulus between compared two objects. The vertical
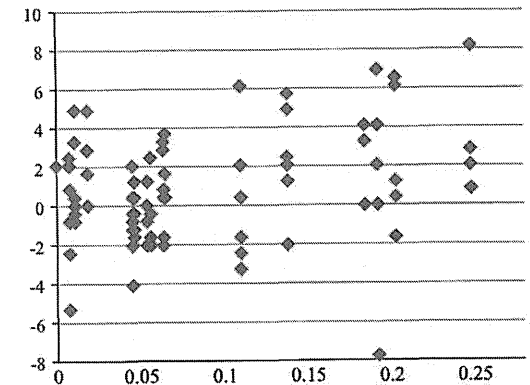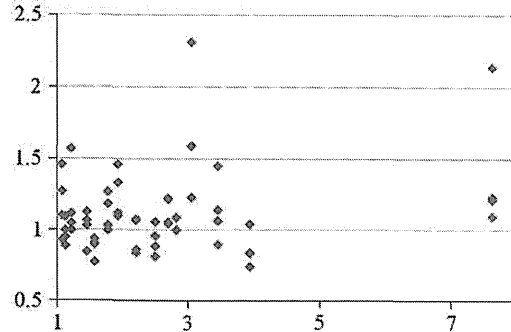
Fig. 3.9 Difference of Young's modulus and contact force

Fig. 3.10 Ratio of difference of Young's modulus and contact force

axis values are differences (Fa−Fb) and ratio (Fa/Fb) of the contact force between compared two objects.

In the figures the negative difference values and the ratio values that are smaller than one in the figures mean that the subjects touch softer object with higher contact force. The differences of the contact force vary widely, and there are some negative values and there are many ratio values that are smaller than one. As mentioned before, the correct answer ratio was about 100 %, therefore, it is said to be difficult to evaluate the tactile softness of the objects with only contact force information.

3.7 Influence of Contact Area Upon Tactile Softness Evaluation

It is confirmed that it is difficult for human to evaluate the tactile softness of the objects with only contact force information. Here, the influence of contact area upon perception of tactile softness evaluation is investigated. We consider that the perception of tactile softness is affected by the contact area information in two ways. One is a size of contact area between subjects' finger and evaluated objects and the other is variation of the contact area size in touch motion. And the latter is investigated.

At first, the relationship between contact force and contact area is investigated. Five subjects push their forefinger into three silicone blocks with ink, in such a way as to evaluate tactile softness of the blocks. The contact force is measured using a pressure sensor that is placed under the object, and the size of contact area between the forefinger and the blocks are calculated using ink blot on the blocks.

Figure 3.11 shows one of examples of the results of the experiment. The sizes of contact area are normalized using that of the softest silicone block. As the results, the size of contact area is depending on the Young's modulus and the size decrease with increase in Young's modulus of the blocks.

Fig. 3.11 Difference of Young's modulus and contact force
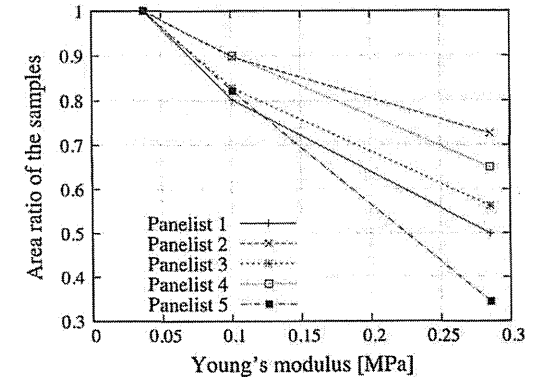
Thus, we focused on the influence of contact area between the finger and an object upon evaluation of tactile softness. Then we tried two sensory tests with four silicones under the different contact condition. Four kinds of silicone softness objects are prepared for the sensory tests. Dimensions of these objects are 30 mm width, 30 mm length, and 20 mm thickness. Young's modulus of the objects in the sensory tests are 0.37, 0.83, 1.01, and 1.47×10^{-1} MPa.

In the sensory tests, two objects are picked out of the four objects, and named object A and object B. Six subjects touch the objects using their forefinger, and compare tactile softness of the objects. The subjects are 20–32 years old men. The sensory tests are conducted in total six combinations of the four objects. Table 3.2 shows the result of the first sensory test. In the table, "s1" to "s6" mean the subjects, and the item of "A" or "B" in "Evaluation of subjects" means the object that the subject evaluated harder. Almost all subjects evaluate that the object with higher Young's modulus is harder.

Next, the subjects evaluate the tactile softness of the objects through the cylinder piston device as shown in Fig. 3.12. The cylinder piston device consists of a piston, and a stage. Shape of the contact 1 is 5 mm square. And that of the contact 2 is 10 mm square. The size of contact 1 is sufficiently-small as compared with the contact area.

Table 3.2 The result of the first sensory test of tactile softness without the piston device

Young's modulus [MPa]		Evaluation of subjects					
Object A	Object B	s1	s2	s3	s4	s5	s6
0.147	0.101	A	A	A	A	A	A
0.147	0.083	A	A	A	A	A	A
0.147	0.037	A	A	A	A	A	A
0.101	0.083	A	A	A	A	A	A
0.101	0.037	A	A	A	A	A	A
0.083	0.037	B	A	A	A	A	A

Fig. 3.12 A cylinder piston device for sensory test
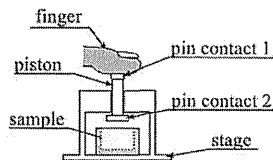
between their forefinger and the objects in the first sensory test. The piston moves vertically in accordance with the motion of a subject's forefinger. The subject pushed the objects using the device to evaluate the tactile softness of the objects. The size of contact area between their forefinger and contact 1 is constant, and the subjects evaluate tactile softness of the object without influence of contact area information. The results of the experiments are evaluated using Scheffse' paired comparison method. At the time, the subjects are asked about the difficulty of the evaluation in the first sensory test without the piston device and the second sensory test with the piston device.

Table 3.3 shows the result in the second sensory test. "Evaluation of subjects" means the object that the subject evaluated harder. Some subjects tend to evaluate that the object with lower Young's modulus is harder. The percentage of the subjects that evaluated the object with higher Young's modulus as harder in all trials is 97.2 % in the first sensory test, but that is 86.1 % in the second sensory test. It was confirmed that all subjects feel it more difficult to evaluate tactile softness of the objects in the second sensory test than that in the first sensory test. These results suggest that the contact area information is important to compare tactile softness difference between slight different objects.

3.8 Design of Sensor for Measuring Touch Sensation

For the development of the sensor system, we have focused on the three points. First point is the motion of the hand/finger. Human changes unconsciously the motion of the hands/fingers depending on the information that we want to know. Lederman et al. have studied the relationship between the information and motion [7].

Table 3.3 The result of the second sensory test of tactile softness using cylinder piston device

Young's modulus [MPa]		Evaluation of subjects					
Object A	Object B	s1	s2	s3	s4	s5	s6
0.147	0.101	A	A	A	A	A	B
0.147	0.083	A	A	A	A	A	A
0.147	0.037	A	A	A	A	A	A
0.101	0.083	A	A	B	A	A	A
0.101	0.037	A	B	A	A	A	A
0.083	0.037	B	A	A	A	A	B

Table 3.4 Information versus motion of finger/hand

Information	Motion of the hand/finger
Texture	Lateral motion
Hardness	Pressure
Temperature	Static contact
Weight	Unsupported holding
Global shape/volume	Enclosure
Global shape/exact shape	Contour following

For example, when we want to know the textures of the objects, we push softly and stroke over the surfaces of the objects. Table 3.4 shows the relationship. These indicate the design of the driving equipment of the sensor system.

Second point is to select the suitable sensor element from many sensor elements. The clarification of the mechanism of the sensory receptor in human skin and touch feelings is useful to consider which information is necessary and as a result sensor elements are chosen. For the sensor system, the chosen sensor element is mounted to driving equipment and the sensor output is obtained. The last one is the signal processing of the sensor output obtained by the sensor system. The signal processing is also derived from the clarification of the mechanism of the sensory receptor in human skin and touch feelings.

3.9 Sensor for Measuring Touch Sensation

Especially, we have focused on the Pacinian corpuscle and we have already developed some tactile sensor systems by using the feature of the Paccini. As mentioned before, Pacinian corpuscle plays important role in high-frequency vibrations that occur when we move our fingertips over structures with very fine texture.

We already tried to measure the tactile sensation of fabrics [8–10], human skin [11–16], hair conditions [17], and we succeeded. Figure 3.13 is the sensor part. PVDF film, polyvinylidene fluoride film is one of the piezoelectric materials. The film is effective to measure a force and displacement and it is used for the sensory material. In addition, PVDF film has features light weight, flexible, sensitive, and thin. The thickness of the film is 28 μm. Furthermore, the film has the feature that the response is very similar to that of Pacinian corpuscle that is one of the receptor of human skin. The lattice shape surface has a role to improve the sensitivity of the sensor as like human finger print.

Figure 3.14 is the one of the sensor system that measures the touch feelings of the fabrics. The sensor part as shown in Fig. 3.13 is attached to the tip of the artificial robotic finger and the sensor is pushed to the surface of the fabric softly by using the piezoelectric actuator. And the sensor is slid over the surface with the x-axis stage driven by a stepping motor. The obtained sensor output is transmitted to personal computer via AD card and the sensor signal is processed.

The typical sensor output is shown in Fig. 3.15.
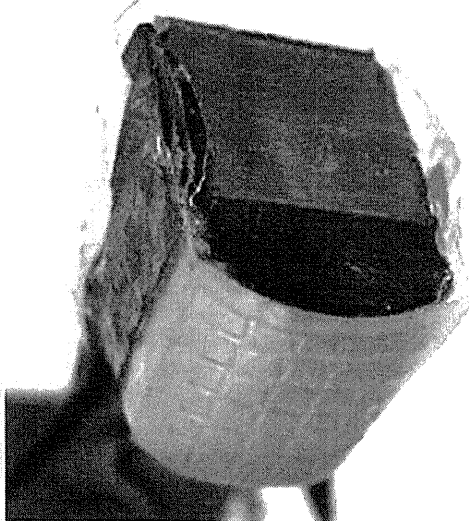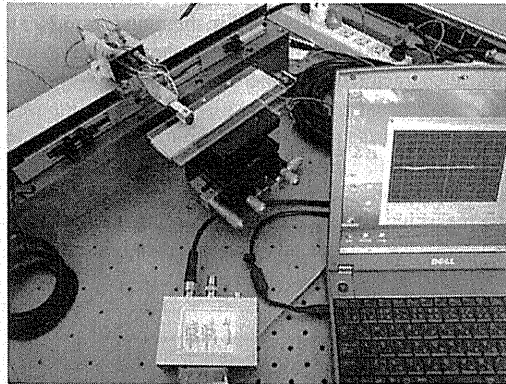
Fig. 3.13 Sensor part

Fig. 3.14 Sensor system

For the signal processing, we calculated two parameters. One is the evaluation of the magnitude of the amplitude of the sensor output, using this equation. This parameter is based on the feature of Pacinian corpuscle, since the output of Pacinian corpuscle is proportional to the applied force.

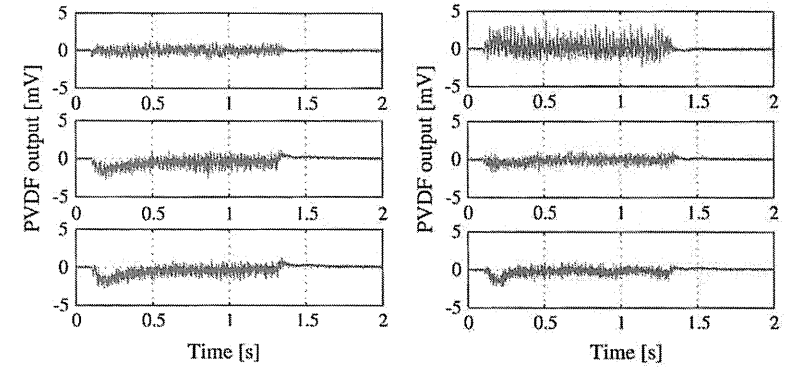$$\mathrm{Var} = \frac{1}{N-1} \sum_{i=1}^{N} (x(i) - \bar{x})^2$$

**Fig. 3.15** Typical sensor output on fabrics

Here, N is the data point number of PVDF output, $x(i)$: ith PVDF output signal, and $\bar{x}$ is the average of PVDF output.

The other is distribution of the power intensity in mid-frequency range Rs. By using the raw data, power spectrum density $P(f)$ was calculated by FFT analysis. Then, the summation is obtained in the range from 100 to 500 Hz, and in the range from 100 to 2,000 Hz. We selected the frequency on the basis of the Pacinian corpuscle characteristics as mentioned before.

$$Rs = \frac{Sa}{Sb}, \ Sa = \sum_{f=100}^{500} P(f), \ Sb = \sum_{f=100}^{2000} P(f)$$

We measured six kinds of women's underwear with this sensor system and two parameters were obtained. The plotted data is shown Fig. 3.16.

Fig. 3.16 *Rs* versus *Var* obtained from the sensor output
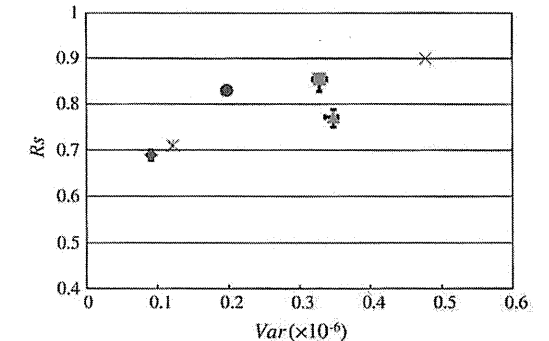
Separating from the measurement experiment, the sensory test was done. Semantic differential (SD) method with five grades scale was used, 14 key words are prepared as follows. 1: Damp–Fine, 2: Rough–Smooth, 3: Prickling–Not prickling, 4: Dry–Moist, 5: Not slimy–Slimy, 6: Not sticky–Sticky, 7: Hanging about–not hanging about, 8: Hard–Soft, 9: Not downy–Downy, 10: Not cool–Cool, 11: Warm–Not warm, 12: Not wet–Wet, 13: Bad feeling–Good feeling, 14: Uncomfortable–Comfortable. Subjects are five women, who are evaluation experts in industry, and they are 30 and 40s.

There are many kinds of analysis method, and we tried factor analysis. The elements of the first principal component are "damp", "moist", "wet", "hanging about", "sticky" and "fitting" and the elements of the second are "downy", "soft", "not prickling", "smooth", "not cool", "warm". The factor loading of the first principal component is larger than 0.9 and the loading of the second is larger than 0.5. And the cumulative contribution ratio of the first and second components is 95 %, and the evaluation of wear and/or touch feeling can be measured by the two components.

The sensor in Fig. 3.15 cannot measure the feelings of "Tight" and "Warm", therefore, as the value of the first component, the average of "damp", "moist", and "wet feeling" is calculated, and as value the second, the average of "soft", "downy", and "not prickling". The values are compared with the sensor output and we obtained the clear relations between Rs and downy and soft feeling whose correlation coefficient is—0.79, and Var and damp and wet feeling is—0.81.

3.10 Palpation Sensor

Palpation sensor for measuring hardness has also been developed [18]. The sensor pushes the object based on the haptics motion in Table 3.4. One example of sensor is shown in Fig. 3.17. PVDF is used also sensory material. And the amplitude
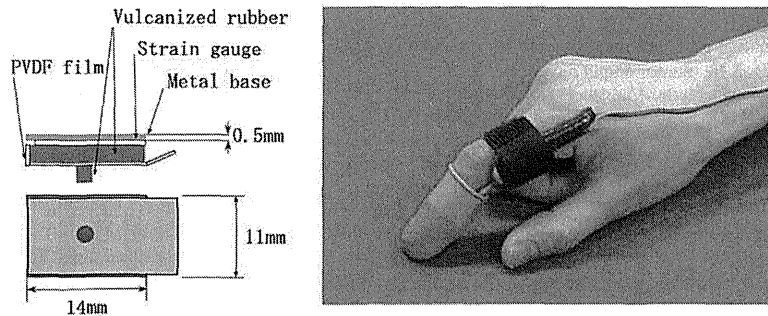

Fig. 3.17 Palpation sensor for measuring prostate

of the output is evaluated. The sensor is attached to the tip of finger and a small-sized motor is attached to the base of the finger to excite the sensor to the object. When the object is harder, the amplitude of the sensor output is larger. We tried to measure the various prostates in clinical tests, such as normal prostate, prostatic cancer, hypertrophy, with stones. The hardness of prostatic cancer is similar to that of bone, and that of prostatic hypertrophy is elastic. Concerning the prostate with stone, the hardness of the part of stone is as same as stone.

Figure 3.18 shows the result that is one example in clinical test. μ means in vertical axis the average of the amplitude of the sensor output. The prostate conditions of subject are as follows. A: Normal and healthy, B: almost normal and healthy, C: between and normal prostatic hypertrophy, D: under treatment of the prostatic cancer, E and F: prostate stones in places, G: prostate stoned.

It is seen that the outputs on subjects A and B are much smaller than the others and the output of B is slightly larger than that of A. The difference corresponds to the difference of the disease A and B.

The sensor value on subject C is much larger than that of subject A and B. It means that the state of the prostate is closer to the hypertrophy. It is seen that the sensor output on subject D, who is under treatment of prostatic cancer, is closer to that of subject C. About the condition of subject D, the palpation result of the doctor without sensor could not distinguish whether the stiffness is that of the prostatic cancer or hypertrophy. The result of the sensor output means the condition is closer to that of prostatic hypertrophy. The sensor output is effective to evaluate the disease conditions.

Subjects E and F have prostate stones in places, and the sensor output takes the maximum and much larger than the others'. Subject G has one prostate stone and it was difficult for the doctor to search for the part. Therefore, the measurements were done many times and the fluctuation of the sensor output was large. From the doctor's diagnosis, the state of prostate except the stone part is prostate hypertrophy. Therefore, the average value became the smaller than that of subject E and F. However, it is noticed the maximum value on subject G is large and the result means that it is unhealthy condition.

Further, the conditions of subjects were investigated using the ultrasound tomography. The enlarged prostate conditions of subject C and D were observed.

Fig. 3.18 Sensor output on prostate glands of subjects A–G
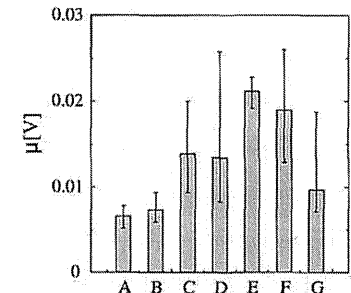
The white marks, which correspond to the prostate stones, were observed in places on the prostate glands of subject E and C. However, the white mark could not be discovered on the prostate of subject G, by ultrasound tomography.

These results showed that the output of the present sensor varies with the stiffness of prostate glands and the present sensor output has a good correlation between doctor's palpation result. Further, it is said the sensor is effective in diagnosing the condition of prostate glands.

3.11 Concluding Remarks

In this chapter, it is shown that the characteristics of human sensory and haptics of hand/finger are useful. In order to make various things that human feel comfortable and good feelings in industry, it is important to know how human feel when he/she use the made things, and the establishment of an objective evaluation method including sensor system is required. In medical welfare fields, the highly accurate palpation sensor is expected to be effective to find the part of disease in early stage and to keep the health. Further, to know the principals and mechanism of the tactile sensation leads to the development of the technology, for example, the tactile display system that can transmit someone else touch feelings and technology that can give reality using of characteristics of touch feelings. In future, the range to use the technology of the touch feelings will extend more and more.

References

1. Shepherd GM (1998) Neurobiology. Oxford University Press, Inc., New York, pp 215–221
2. Sumiko N (1970) A transform of scheffe AN" s method (Japanese), In: Proceeding of 11th sensory test conference, Union of Japanese Scientists and Engineers
3. Yoshikawa Y (1975) Mechanical behavior of skin and measurement way (hardness measurement of a living body and artificial judge < special story>). Meas Control 3(14):263–280
4. Kazuo Y, Hidehiko T, Shotaro O (1975) Physical characteristics of human finger. Biomechanisms 3:27–36
5. Fung YC (1993) Biomechanics: mechanical properties of living tissues, 2nd edn. Springer, New York
6. Maeno T, Kobayashi K, Yamazaki N (1997) Relationship between the structure of finger tissue and the location of tactile receptors. Trans Jpn Soc Mech Eng Series C 63(607):881–888
7. Lederman SJ, Klatzky RL (1987) Hand movements: a window into haptic object recognition. Cognitive Psychology 19:346. Copyright 1987 by Elsevier
8. Tanaka M (2002) Measurement and valuation of touch sensation: texture measurement on underclothes. Stud Appl Electromagnet Mech 12:53–58
9. Tanaka M, Numazawa Yu (2004) Rating and valuation of human haptic sensation. Int J Appl Electromagnet Mech 19:573–579
10. Tanaka Y, Tanaka M, Chonan S (2007) Development of a sensor system for collecting tactile information. Microsyst Technol 13:1005–1013
11. Tanaka M, Tanaka Y, Chonan S (2008) Measurement and evaluation of tactile sensations using a PVDF sensor. J Intell Mater Syst Struct 19:35–42

12. Tanaka M (2001) Development of tactile sensor for monitoring skin conditions. J Mater Process Technol 108:253–256
13. Tanaka M, Hiraizumi J, Leveque JL, Chonan S (2002) Haptic sensor for monitoring skin conditions. Int J Appl Electromagnet Mech 14:397–404
14. Tanaka Mami, Leveque JL, Tagami H, Kikuchi K, Chonan S (2003) The "Haptic finger"-a new device for monitoring skin condition. Skin Res Techonol 9:131–136
15. Tanaka M, Sugiura H, Leveque JL, Tagami H, Kikuchi K, Chonan S (2005) Active haptic sensation for monitoring skin conditions. J Mater Process Technol 161:199–203
16. Tanaka M, Matsumoto M, Uetake N, Kikuchi K, Leveque JL, Chonan S (2006) Development of an active tactile sensor for measuring human skin conditions. In: Sixteenth international conference on adaptive structures and technologies, pp 335–341 (DEStech Publications Inc.)
17. Okuyama T, Hariu M, Kawasoe T, Kakizawa M, Shimizu H, Tanaka M (2011) Development of tactile sensor for measuring hair touch feeling. Microsyst Technol 17:1153–1160
18. Tanaka M, Furubayashi M, Tanahashi Y, Chonan S (2000) Development of an active palpation sensor for detecting prostatic cancer and hypertrophy. Smart Mater Struct 9:878–884

Examination of Superimposed Signal and Power Transmission System in Direct Feeding FES

*T. Oikawa, *Non-Member, IEEE*
**Y.Ota, **T. Takura, **F. Sato, *H. Matsuki, *Member, IEEE*
T. Sato, Non-Member, IEEE

Abstract—In this paper, we applied Superimposed Signal and Power Transmission System to direct feeding FES and show that this system can transmit power signal and communication signal at the same time.

I. INTRODUCTION

Effectiveness of reconstructing motor function with functional electrical stimulation (FES) is confirmed by recent nerve engineering field development. We have studied direct feeding FES using electromagnetical near field to realize less invasive and high precision stimulation [1]. Direct feeding FES is comprised of extracorporeal device and miniature implant stimulators. In fact, direct feeding FES is using two coils to transmit power signal and communication signal. However, There are problems of physical interference between the coil and growing device due to use two coils. Therefore, in this study, we aim at the realization of direct feeding FES using superimposed signal and power transmission system [2] performing feeding and communication with a single coil at the same time.

II. SUPERIMPOSED SIGNAL AND POWER TRANSMISSION SYSTEM

We show a diagrammatical view of superimposed signal and power transmission system in Fig. 1. This system uses an electricity signal as a carrier wave. It modulates carrier signal showing implant channel and stimulation intensity, transmits extracorporeal coil to internal coil. It uses phase shift keying (PSK) modulation. The internal device receives modulation wave and sends it to power feeding unit and communication unit. Power feeding unit commutates modulation wave and gets direct voltage to use implant stimulators.
Communication unit regenerates carrier signal to demodulate modulation wave and discerns implant channel and control stimulation intensity.

III. EXPERIMENT AND RESULT

We transmitted modulation wave from extracorporeal device to implant stimulators and generated stimulation voltage and stimulation pulse. We used 50 turn solenoidal coil for

*T. Oikawa, T. Sato, H. Matsuki are with Graduate School of Biomedical Engineering, Tohoku University, Sendai, Miyagi 980-5879 JAPAN (corresponding author to provide phone: 022-795-7059; fax: 022-263-9307; e-mail: matsuki@ecei.tohoku.ac.jp).
** T. Takura and F. Sato are with Graduate School of Engineering, Tohoku University, Sendai, Miyagi 980-5879 JAPAN.

extracorporeal coil, and these diameters were 90 mm, and the lengths ware 110 mm. The implanted coil was 150 turns solenoid coil, and has a Mn–Zn ferrite core sized of 0.7 by 0.7 by 10 mm. The communication speed assumed it 25 kHz in consideration of reaction velocity of human, and modulated by a carrier wave of 10 times. The result of experimentation in Fig. 2. It is stimulation voltage (10 V), carrier signal, modulation wave, stimulation pulse from the top. This system can transmit power signal and communication signal at the same time. Consumed power of implant stimulators is 240 mW when it stimulates, 60 mW when it waits. Circuit load is 60 Ω when it stimulates, 2.4 kΩ when it waits.
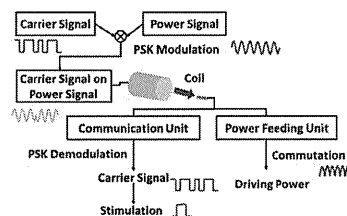

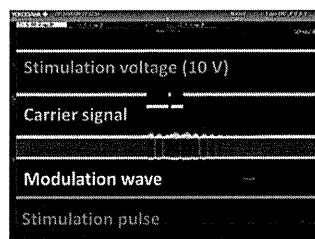Figure 1. Superimposed Signal and Power Transmission System.

Figure 2. Output of implant stimulators.

REFERENCES

[1] K.Kato, T.Sakamaki, T.Sato, T.Takura, F.Sato, H.Matsuki, K.Seki and Y.Handa, "Bidirectional Communication System for Magnetic Direct Feeding FES", IEEE Transactions on Magnetics, Vol.47, No.10, October, 2011.

[2] S. Matsumura, K. Kato, Y. Kohata, T. Sakamaki, T. Takura, F. Sato, H. Matsuki, K. Seki, Y. Handa, and T. Sato, "Assessment of Superimposed Signal and Power Transmission System in Implanted TES", Journal of the Msagnetics Society of Japan Vol. 34, No. 3, 2010.

Development of Novel Flow Chamber to Study Endothelial Cell Morphology: Effects of Shear Flow with Uniform Spatial Gradient on Distribution of Focal Adhesion*

Daisuke YOSHINO**,†, Naoya SAKAMOTO***,††, Keita TAKAHASHI****,
Eri INOUE** and Masaaki SATO**,***

**Graduate School of Biomedical Engineering, Tohoku University
6-6-01 Aramaki-Aoba, Aoba, Sendai 980-8579, Japan
E-mail: yoshino@plasma.ifs.tohoku.ac.jp
***Graduate School of Engineering, Tohoku University
****School of Engineering, Tohoku University
Present Address: † Institue of Fluid Science, Tohoku University
†† Kawasaki University of Medical Welfare

Abstract

Fluid shear stress (SS) is well known to cause morphological changes in vascular endothelial cells (ECs) accompanied by alteration in actin cytoskeletal structure and distribution of focal adhesions. Recent studies have shown that spatial SS gradient also has effects on EC morphology, but the detailed mechanisms of EC responses to SSG remain unclear. In the present study, we sought morphological responses of ECs under SS and uniform SSG condition using a newly developed flow chamber. Confluent ECs were exposed to SS with SSG for 24 hours. Focal adhesions of the EC under SS without SSG were localized in the cell periphery. In contrast, focal adhesions were expressed not only in the periphery but also in interior portion of cells after exposure to SS with SSG. Unlike ECs exposure to SS developed thick actin filaments aligned to the direction of flow no development of thick actin filaments but thin and short filaments were observed in ECs after 24-hour exposure to SS with SSG. Since the distribution of focal adhesion is of critical importance for development of actin filaments and cell morphological changes, these results suggest that SSG suppresses redistribution of focal adhesions, resulting in the inhibition of EC morphological changes and development of thick actin filaments in response to flow.

Key words: Endothelial Cells, Shear Stress, Shear Stress Gradient, Focal Adhesion, Cytoskeleton

1. Introduction

Vascular endothelial cells (ECs), lining on the luminal wall of blood vessels, change their morphology and regulate a variety of physiological functions of vessel walls in response to hemodynamic stimuli such as fluid shear stress (SS) in vivo. There have been many previous studies that have investigated responses of ECs to SS and shown that ECs elongate and align to the direction of flow in response to physiological levels of SS (1~2 Pa) [1]. Previous studies have also shown that magnitude of SS influences EC morphology and

may provoke various cellular functions that play important roles in vascular homeostasis [2,3].

It was also found that cytoskeleton and focal adhesion have important roles in EC morphology. A number of actin filaments, which is one of the cytoskeletons, grow to actin stress fibers aligned to the direction of flow in ECs exposed to SS [4]. Focal adhesion is the protein complex through which the cytoskeletons connect to extracellular matrix. This complex consists of integrin, vinculin, talin, paxilin, focal adhesion kinase (FAK), and so on. Paxillin is particularly thought to play an important role in responses of ECs to mechanical stimuli. In a EC exposed to fluid flow, there is difference in phosphorylated state of paxillin between upstream and downstream within the cell [5], suggesting that differences in the expression level and phosphorylated state of paxillin within an EC influence morphological changes of ECs.

Recently, spatial SS gradient (SSG) has also attracted a great deal of attention as a key factor for EC morphology under flow conditions. Szymanski et al. [6] exposed SS (0~20.6 Pa) and SSG (-9~14 Pa/mm) using a T-shaped flow chamber mimicking arterial bifurcations, and showed that ECs density was increased at the high SS and high SSG region. Sakamoto et al. exposed high SS (~16 Pa) and high SSG (~34 Pa/mm) using the T-chamber, and showed SSG suppressed the orientation of ECs [7]. However, it is too complicated to evaluate effects of SSG on EC morphology by using T-chamber because it is very difficult to control the combination of SS and SSG in the T-chamber. Although a recent study developed a flow chamber which has converging and diverging channel to create well-defined SSG condition [8], the magnitude of SSG in the chamber was much lower compared with the previous studies, and knowledge of morphological responses of ECs to combination of SS and SSG is still limited.

In the present study, we develop a novel flow chamber, which can generate uniform spatial SS gradient, for evaluating effects of SSG on endothelial morphology. Using the developed chamber, we observe changes in cytoskeletal structures and distribution of focal adhesions of ECs, and discuss the effect of SSG on morphology of ECs.

2. Design of novel flow chamber for generating uniform shear stress gradient

SS (=τ) occurring in a parallel-plate flow chamber is defined by the following equation [9].

$$\tau = \frac{6Q\mu}{wh^2},\qquad(1)$$

where Q is flow rate, μ is fluid viscosity of culture medium, w is width of a flow channel, and h is a channel height. Equation (1) is also valid for Newtonian fluid in fully developed laminar flow in a flow channel with a high aspect ratio ($w \gg h$) [8]. Therefore, we considered a flow channel with a wide and low roof in a newly designed flow chamber as illustrated in Fig. 1A. The flow channel consists of three regions: an "entrance" region, a "gradient" region, and an "exit" region. The length of each region is denoted as L_{en}, L_g, or L_{ex}. The heights of "entrance" and "exit" regions are denoted as h_0 and t, respectively. In addition, the channel height in the "gradient" region is defined by the function $h(x)$. Distance from the ideal origin of the function $h(x)$ to the start point of "gradient" region is indicated as L_0. By considering linear increase in SS, $h(x)$ is set up as follow:

$$h(x) = t\sqrt{\frac{L_g + L_0}{x + L_0}}.\qquad(2)$$

SS and SSG (=$d\tau/dx$) are given by following equations:

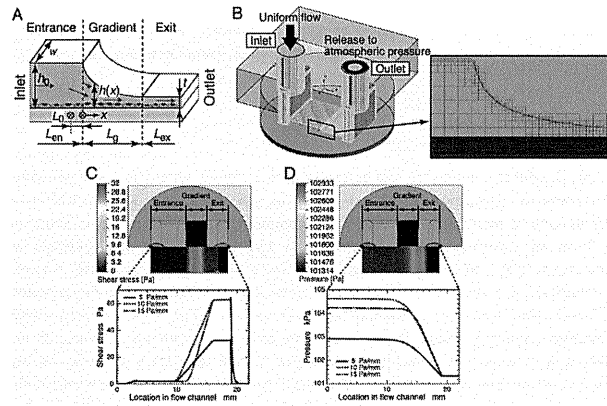$$\tau = \frac{6Q\mu}{wt^2(L_g + L_0)}(x + L_0),\qquad(3)$$

Fig. 1 The developed flow chamber that can generate uniform spatial SS gradient. (A) Schematic illustration of flow channel in the developed chamber. (B) Boundary conditions and the mesh model used for CFD simulation. (C) Simulated distribution of shear stress in flow channel. (D) Simulated distribution of pressure in flow channel.

$$\frac{d\tau}{dx} = \frac{6Q\mu}{wt^2(L_g + L_0)}. \tag{4}$$

The maximum and minimum SS values in the flow channel are obtained as follows:

$$\tau_{max}\big|_{x=L_g} = \frac{6Q\mu}{wt^2}, \tag{5}$$

$$\tau_{min}\big|_{x=0} = \frac{6Q\mu L_0}{wt^2(L_g + L_0)}. \tag{6}$$

The length L_g of the "gradient" region and L_0 are derived by using above equations.

$$L_0 = \tau_{min} \Big/ \left(\frac{d\tau}{dx}\right) \tag{7}$$

$$L_g = (\tau_{max} - \tau_{min}) \Big/ \left(\frac{d\tau}{dx}\right) \tag{8}$$

The lengths of "entrance" and "exit" regions can be arbitrarily defined within a range of the flow channel length, which depends on the size of a dish. Once a designer gives the value of maximum SS, minimum SS, and SSG, dimensions of the required flow chamber are determined. In the present study, a flow chamber designed using the theory described above is named as the "derivative constant" chamber (D chamber). We designed 3 types of D chambers that can generate SSG values of 5, 10, and 15 Pa/mm, respectively. Table 1 presents dimensions of main design parameters of the D chamber. The length L_{en} of "entrance" region was set up to be sufficient to develop a boundary layer before "gradient" region by using a computational fluid dynamics (CFD) simulation described below.

In order to confirm the performances of the D chambers, the CFD simulation was performed by the finite volume method in SolidWorks Flow Simulation (Dassault Systèmes SolidWorks Corporation). Culture medium perfused in the chamber was modeled with the continuity equation and the Navier-Stokes equation for an incompressible Newtonian fluid. The mass density and viscosity of culture medium were set to 1000 kg/m³ and 7.4×10^{-4} Pa·s, respectively, and the flow rate was set to 259 (5 Pa/mm), 503 (10 Pa/mm), or 402 ml/min

Table 1 Dimensions of main design parameters of the D chamber

Design Parameter	5 Pa/mm	10 Pa/mm	15 Pa/mm
Length of "entrance" region L_{en} (mm)	7	7	9
Length of "gradient" region L_g (mm)	6	6	4
Length of "exit" region L_{ex} (mm)	3	3	3
Distance from the ideal origin of the function $h(x)$ to the start point of "gradient" region L_0 (mm)	0.40	0.20	0.13
Width of flow channel w (mm)	15	15	12
Height of "entrance" region h_0 (mm)	0.80	1.11	1.11
Height of "exit" region t (mm)	0.20	0.20	0.20

(15 Pa/mm). The flow rate profile was defined as the uniform flow, and it applied to the inlet of flow channel as a boundary condition. The pressure at the outlet boundary was set to the atmospheric pressure. We used the mesh of hexahedron cells for CFD simulation, and the number of computational cells was 471906 (5 Pa/mm), 495216 (10 Pa/mm), or 482401 (15 Pa/mm). The configurations for CFD simulation described above are summarized in Fig. 1B. The CFD results are shown in Fig. 1C, D. The SS in the figure indicates the value on the center line of bottom surface in the flow channel. In the D chamber with 5 Pa/mm SSG, SS increased from 2 Pa to 32 Pa while SS value in D chambers with 10 and 15 Pa/mm increased from 2 Pa to 62 Pa. It was confirmed that linear increase in SS could be kept within the "gradient" region excluding edges of the flow channel. The Reynolds number in the flow channel was 779 (5 Pa/mm) or 1510 (10 Pa/mm and 15 Pa/mm), respectively. Performances of the D chambers could be confirmed by using CFD simulation. In this paper, the D chamber with 15 Pa/mm was used for flow-exposure experiments because SSG could come to 15 Pa/mm at the arterial bifurcation [10].

3. Materials and Methods

3.1 Cell culture

Human carotid artery endothelial cells (HCtAECs; Cell Applications) were cultured with Medium 199 (Invitrogen) containing 20 % heat-inactivated fetal bovine serum (SAFC Bioscience), 10 µg/l human basic fibroblast growth factor (AUSTRAL Biologicals), and 0.1 % penicillin/streptomycin (Invitrogen). HCtAECs from 5th to 9th passages were cultured in 35 mm diameter glass-based dish (Iwaki) pre-coated with 0.1 % bovine gelatin (Sigma-Aldrich), and used for the experiments.

3.2 Flow-exposure experiment

The flow chamber was connected to a flow circuit comprising a roller pump (Master Flex) and two reservoirs, as illustrated in Fig. 2. The flow circuit was filled with the same medium as that used during cell culture. One reservoir was open to the atmosphere, and the culture medium in the flow circuit was equilibrated with 93 % air and 7 % CO_2 to maintain pH at 7.4. The system was maintained at 37 °C with a temperature-controlled bath. For the experimental condition of SS with/without SSG, we used the newly designed flow chamber and a parallel-plate flow chamber [11], respectively. We focused on the cells exposed to the following combinations of SS and SSG; SS = 2 and 6 Pa, and SSG = 0 and 15 Pa/mm. Distance from the start point of "gradient" region to the position of observation is 0 mm (SS = 2 Pa) or 0.27 mm (SS = 6 Pa) in case where SSG is 15 Pa/mm. The SS values were determined as levels of physiological and high shear conditions by reference to previous studies [12, 13].
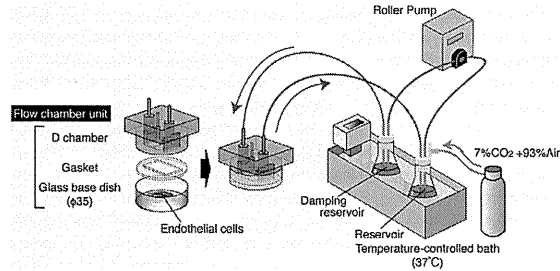
Fig. 2 Flow-exposure system consisting of a flow chamber, a roller pump, two reservoirs, and temperature-controlled bath.

3.3 Fluorescent staining

After 24-hour flow exposure, ECs were fixed with 4 % paraformaldehyde phosphate buffer solution (Wako Pure Chemical Industries) for 15 minutes at room temperature and washed thrice with PBS (Dulbecco's PBS(-); Nissui Pharmaceutical). EC membranes were then permeabilized with 0.1 % Triton X-100 (Wako Pure Chemical Industries) for 5 minutes. After washing thrice with PBS, ECs were then treated with Block Ace (DS Pharma Biomedical) for 45 minutes to prevent the non-specific adsorption of antibody. ECs were subsequently incubated with anti-mouse paxillin monoclonal antibody (BD Biosciences) and anti-rabbit VE-cadherin antibody (eBioscience) for an hour and a half, followed by secondary antibodies conjugated with anti-mouse Alexa Fluor 488 (Invitrogen) and anti-rabbit Alexa Fluor 633 (Invitrogen) for 1 hour. For staining nuclei and actin filaments, ECs were incubated with DAPI (Invitrogen) for 5 minutes, and Alexa Fluor 546 phalloidin (Invitrogen) for 20 minutes, respectively. Fluorescent images of paxillin, VE-cadherin, nuclei, and actin filaments were observed with an inverted confocal laser scanning microscope (Olympus).

3.4 Evaluation of focal adhesion distribution

It is important for evaluating localization of paxillin among the variously-sized ECs to normalize the sizes of the ECs. We firstly treated the fluorescent images to remove non-specific noises by using the discriminant analysis method. The outlines of ECs were extracted from the fluorescent images, and then the ellipsoids equivalent to ECs shapes were computed based on the extracted outlines by using ImageJ (National Institute of Health). Here, we achieved the central coordinate, lengths of major and minor axses, and orientation angle of the ellipsoid equivalent to the ECs. Then, areas and coordinates of paxillin in the extracted ECs were obtained by using the function of "Analyze Particles." The ellipsoids equivalent to the ECs were normalized to unit circles by using the dimensions of the ellipsoid. The coordinates of paxillin were converted from rectangular coordinates to polar coordinates, and we finally normalized coordinates of paxillin and trabscribed onto a unit circle. In addition, an expressed area of paxillin was highlighted with six levels of circular sizes.

4. Results

4.1 Cell morphology and cytoskeletal structure

Figure 3 shows fluorescent images of ECs after 24-hour flow exposure. ECs maintained
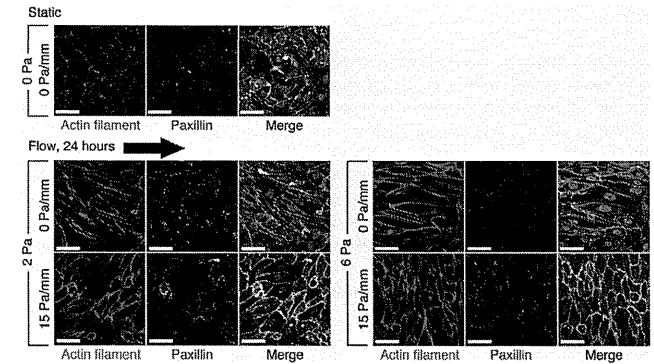
Fig. 3 Representative fluorescent images of ECs exposed to the combination of SS and uniform SSG for 24 hours. Red: actin filament, green: paxillin, bule: nucleus, white: VE-cadherin. "Merge" indicates the image merged with fluorescent images of actin filament, paxillin, nucleus, and VE-cadherin. Bar = 50 μm.
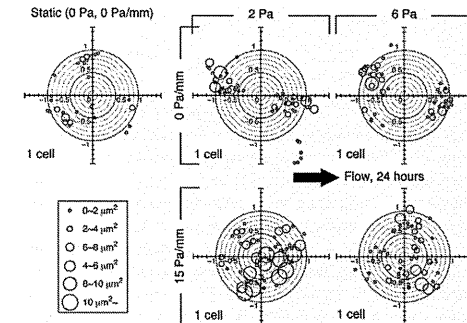

Fig. 4 Representative distributions of paxillin in ECs exposed to the combination of SS and uniform SSG for 24 hours.

a confluent monolayer, and formation of intercellular gaps, detachment, and damage were not observed in any of the experimental conditions. ECs exposed to SS without SSG elongated and oriented in the direction of flow. Actin filaments existing along the periphery of ECs developed and became thick. On the other hand, ECs under the condition of SS with SSG did not elongate and orient in the direction of flow. Actin filaments in the periphery of cells remained thin, and the thin and short filaments were formed in the interior portion of the cell.

4.2 Distribution of paxillin in cell under shear stress with/without its spatial gradient

Based on fluorescent images in Fig. 3, we evaluated distribution of paxillin in ECs by using the method described in section 3.4. The representative distribution of paxillin in an EC exposed to each flow condition is shown in Fig. 4. Figure 5 shows histograms obtained by counting the number of paxillin from the center to the periphery of an EC. Paxillin in